ACTUATORS

# Linear and rotational microhydraulic actuators driven by electrowetting

**Jakub Kedzierski* and Eric Holihan**

**Microhydraulic actuators offer a new way to convert electrical power to mechanical power on a microscale with an unmatched combination of power density and efficiency. Actuators work by combining surface tension force contributions from a large number of droplets distorted by electrowetting electrodes. This paper reports on the behavior of microgram-scale linear and rotational microhydraulic actuators with output force/weight ratios of 5500, cycle frequencies of 4 kilohertz, <1-micrometer movement precision, and accelerations of 3 kilometers/second$^2$. The power density and the efficiency of the actuators were characterized by simultaneously measuring the mechanical work performed and the electrical power applied. Maximum output power density was 0.93 kilowatt/kilogram, comparable with the best electric motors. At maximum power, the actuator was 60% efficient, but efficiencies were as high as 83% at lower power. Rotational actuators demonstrated a torque density of 79 newton meters/kilogram, substantially more than electric motors of comparable diameter. Scaling the droplet pitch from 100 to 48 micrometers increased power density from 0.27 to 0.93 kilowatt/kilogram, validating the quadratic scaling of actuator power.**

## INTRODUCTION

The conversion of electrical to mechanical power is an important part of many technologies ranging in size from cars to electric toothbrushes and affecting many aspects of our lives. For large systems, electric motors comprise the vast majority of electrically driven actuators. Motors are efficient and have a relatively high power density, and the technology they rely on is very well developed. However, for all their advantages, motors have serious drawbacks: They are heavy, hard, and inflexible, and they do not scale to small dimensions. Inductive actuators such as classical motors rely on coils of wire that increase in resistance as the scale of the actuator shrinks; eventually, the resistive component becomes dominant. This effect occurs rapidly at the gram scale, with 0.5-g motors being only 0.5% efficient (*1*, *2*). On a microscale, piezoelectric actuators are widely used (*3*–*6*), but they are often difficult to integrate. In addition, piezoelectric actuators and classical motors are heavy and lack flexibility. A light, flexible actuator, like biological muscle, is required for soft robotics, wearable devices, and many biomedical applications. Work on artificial muscle is an active area of research and has produced some very interesting technologies. Electroactive polymers (*7*–*9*), thermally actuated materials (*10*), pressure transducers (*11*, *12*), and others have exhibited some of the desirable characteristics of muscle. However, a combination of high power density and efficiency has been particularly difficult to obtain. Only recently have electrohydraulic muscle (*13*, *14*) and microhydraulic actuators (*15*, *16*) demonstrated this combination in soft materials. Microhydraulic actuators consist of thin layers of solid sheets separated by fluidic drops and move these layers relative to each other by internally modifying surface energy with electrowetting. They borrow in form and function from several actuating technologies, including capillary motors (*17*), electrowetting conveyors (*18*), multicycle electrostatic actuators (*19*, *20*), stepper motors, and biological muscle. In addition to offering high power and efficiency, microhydraulic actuators increase quadratically in power density when scaled to smaller dimensions and work at a relatively low voltage (*15*).

In this paper, we present several notable steps in the development of microhydraulic actuators. We validated the quadratic scaling of power density as a function of droplet frequency by comparing the behavior of 48-μm droplet pitch technology to the results obtained for a 100-μm pitch version (*15*). With simultaneous measurement of mechanical output-power and electrical input-power, we demonstrated a power density of 0.93 kW/kg, an order of magnitude higher than muscle (*21*, *22*), with a high power conversion efficiency of 60%. We also present rotational microhydraulic actuators, which functioned like stepper motors, giving fine angular precision of motion down to 0.03° and a torque of 84 μNm. Although microhydraulics may find applications in various areas, its applications in robotics, particularly microrobotics, could be most effective. A recent list of grand challenges in robotics (*23*) featured active, efficient, and compliant materials assembled with new techniques as the first challenge (*24*) and bioinspired designs as the second. Microhydraulic actuators are a soft, muscle-like, self-assembling material, which may be able to address these challenges and produce powerful, small-scale robots.

### Actuator operation

Microhydraulic actuators, shown in Fig. 1, work by integrating force contributions generated by the surface tension of water drops deformed by electrowetting (*25*, *26*) electrodes. Forces integrated along a thin layer of polyimide, the droplet array, which held the droplets in hydrophilic grooves, at a fixed pitch, $D_{\text{pitch}}$, of 48 μm. Each drop contributed only a small surface tension force to the array, but with a large number of microscopic drops, the net force can be relatively large. The electrodes were also arranged in a regular array, with four distinct phases, P1 to P4, repeating in a cyclic pattern. The cycle pitch is the same as the droplet pitch, whereas the pitch of individual electrodes is $D_{\text{pitch}}/4$ or 12 μm. When the droplets are asymmetrically deformed by electrowetting, the integrated surface tension force moves the droplet array relative to the electrode array. The net force of the actuator is linearly proportional to the number of drops and their width. It can be estimated as $\gamma W_{\text{total}}$, with $\gamma$ being the surface tension of the water/oil interface and $W_{\text{total}}$ the total width of all the drops. Phases are switched at the step frequency $F_{\text{step}}$, and because there are four steps in a cycle, the cycle frequency, $F_{\text{cyc}}$, is $F_{\text{step}}/4$. The droplet array moves at a veloc-

---

Massachusetts Institute of Technology Lincoln Laboratory, Lexington, MA 02420, USA.
*Corresponding author. Email: jakub@ll.mit.edu

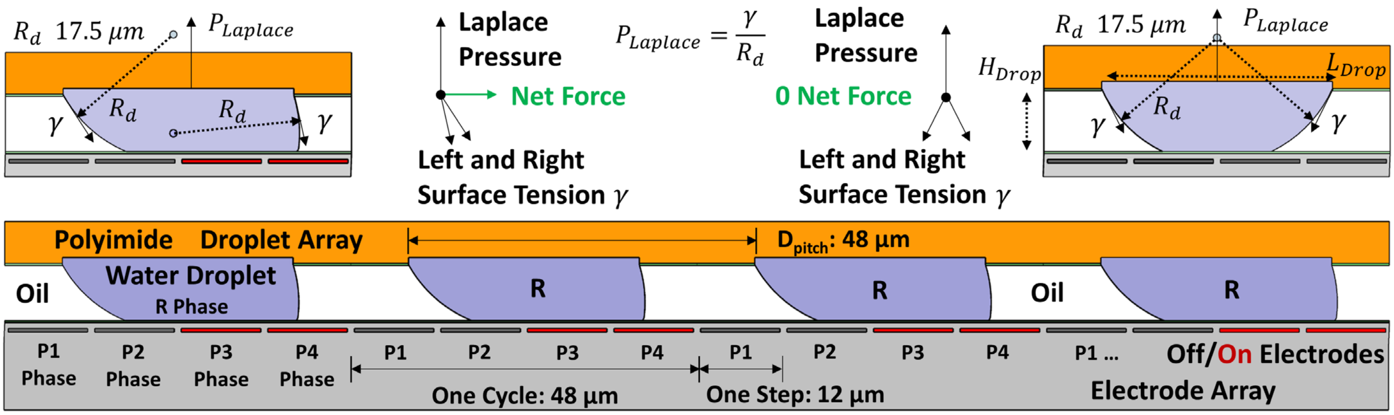

**Fig. 1. Actuator operation.** Functional two-dimensional cross section of a linear microhydraulic actuator, drawn to scale, with the water droplets deformed by voltages on electrodes (P3,P4), relative to the water droplet voltage *R*. The polyimide droplet array is shown in orange, 8 M LiCl water drops are shown in blue, the dodecane oil between drops is shown in white, the electrode array dielectric is shown in light gray, and the electrodes are shown in gray and red for 0 and 40 V, respectively. (**Top right**) Droplet profile with the electrodes off. In this condition, the net forces on the array are zero. (**Top left**) When the droplets are deformed by the electrodes, a net horizontal force is produced, and the droplet array moves to align the drops to the energized electrodes. The energized electrodes are cycled with two on at any particular time, going through four states—(P1,P2), (P2,P3), (P3,P4), and (P4,P1)—at which point the cycle starts again at (P1,P2). The droplet array physically follows the energized states to result in actuator motion. For motion in the opposite direction, the order of the states in the cycle is reversed. The oil-water surface tension, γ, is 55 mJ/m$^2$.

ity of $D_{pitch}F_{cyc}$. The droplet array motion can be smooth or discrete depending on frequency and voltage; generally lower frequencies and higher voltages result in discrete motion as the array moves to the new step position and stops at each step. The velocity of the actuator can fall below $D_{pitch}F_{cyc}$ or stop completely if the actuation starts skipping steps; this occurs if the $F_{cyc}$ is too high, the external load is too high, or the actuation voltage is too low.

$D_{pitch}$ is an important parameter that determines many properties of the actuator; in this paper, a $D_{pitch}$ of 48 μm was used. When actuated, the droplet contact length on the electrode array should be approximately two electrodes long, or 24 μm, and the centers of curvature of the drops should average to be in the polyimide for droplet stability. These constraints led to a droplet length, $L_{drop}$, of 32 μm. The droplet height, $H_{drop}$, should be as high as possible to reduce viscous losses while still maintaining drop stability. The upper limit for $H_{drop}$ is half the droplet length or 16 μm. During assembly, the droplet Laplace pressure was set to 3.1 kPa, corresponding to a droplet radius of 17.5 μm and $H_{drop}$ of 10 μm.

### Fabrication and assembly

The fabrication of the actuator components, the electrode, and the droplet arrays is detailed in Materials and Methods and the Supplementary Materials. The electrode array consisted of a series of electrodes patterned in metal and covered by a hydrophobic dielectric, which was patterned with rail-shaped contacts that bias the droplet array. The droplet array consisted of a 5-μm-thin layer of polyimide, with a patterned fluoropolymer layer used to define the hydrophilic droplet regions. All the actuating droplets were topologically connected to each other and to a reference rail droplet (see Fig. 2). Once the dry components were fabricated, they needed to be wetted and assembled. The wetting and the assembly of the 5-μm-thin polyimide layers were not trivial. At this ultrathin scale, electrostatics dominated, and any static charge on the polyimide caused it to bend or fly away and stick to the nearest object. Peeling the polyimide off the wafer after fabrication generated enough static charge to make it very difficult to handle, unless it was immediately neutralized by using a spot charge neutralizer. Another challenge was water evaporation. Water droplets on a 30-μm scale evaporate in approximately 10 ms at standard laboratory humidity and temperature. Working at or near the dew point can extend this (*15*), but it is very difficult to extend the evaporation time to minutes, which is required for assembly. To eliminate evaporation, we used 8 M LiCl water as the water phase. LiCl depresses the vapor pressure of water so that it does not evaporate completely until the humidity falls below 11% (*27*). At the 40% humidity used in our laboratory, 8 M LiCl water droplets just equilibrated with ambient humidity, and even micrometer-sized drops lasted for months. Relative to pure water, the equilibrium of LiCl at 40% humidity resulted in approximately 10% higher density and surface tension and roughly doubled the viscosity. The use of LiCl also solved another important problem: the evaporation of water through the oil phase after assembly. Handling was another challenge. The thin layers were manipulated with small custom-made vacuum wands built from blunt syringe tips. Neutralized and wetted droplet arrays for both linear and rotational actuators are shown in Fig. 2.

Details of the assembly process are described in Materials and Methods and the Supplementary Materials. As the last part of the assembly, the droplet array self-aligned to the electrode array. Horizontal and angular registration occurred when the rail drop, shown in Figs. 2 and 3, aligned to the hydrophilic regions in the electrode array. Vertical alignment was set by the droplet height. This way, the actuator components self-aligned (*28*) in all but the actuating direction. Figure 3 shows the top view of the actuator after assembly. Grounding of the droplets is particularly important. As can be seen on the left of Fig. 3, the droplets were biased through the reference phase R at a negative voltage $V_t$. Electrical connection between the phase rail and the reference droplet occurred through a Pt contact. Because the droplet was capacitively insulated from the other phases P1 to P4, the reference rail and thus the Pt contact conducted only alternating current, avoiding electrolysis.

## RESULTS

### Electrical characterization

Actuation was typically done at an electrode phase voltage of 37 V for $V_b$ and a reference droplet voltage of −19 V for $V_t$. The variables for the droplet reference voltage and the phase voltage, $V_t$ and $V_b$, respectively,

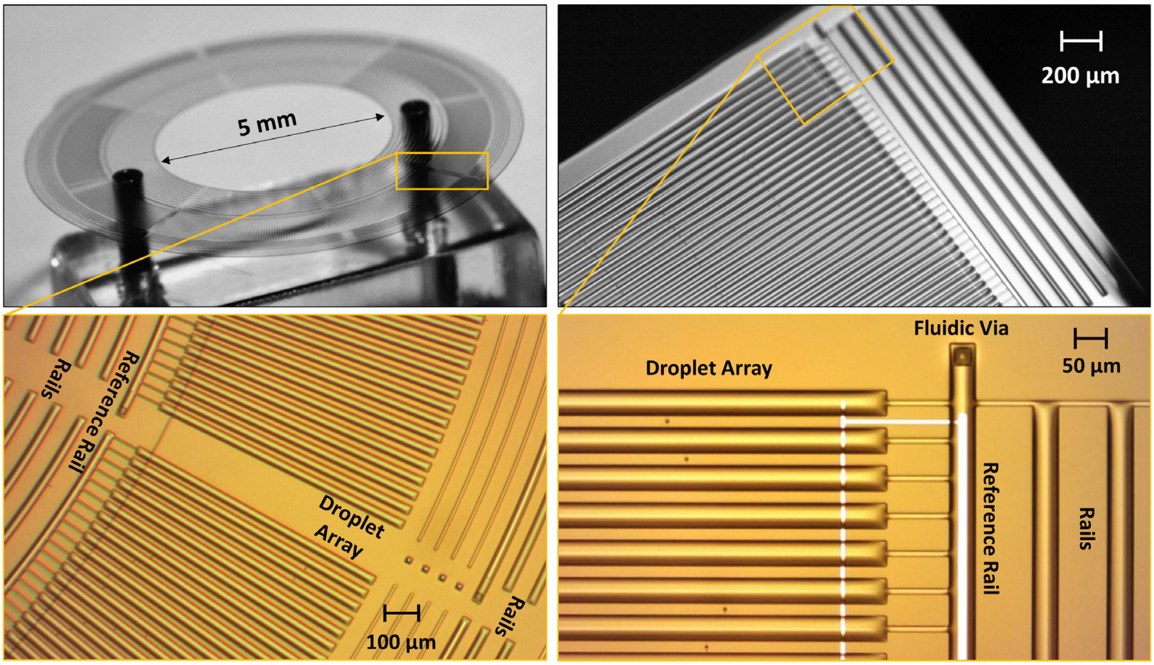

**Fig. 2. Polyimide droplet array.** Optical micrographs of polyimide droplet arrays wetted with 8 M LiCl. (**Left**) Rotational actuator array. (**Right**) Linear actuator array. Droplet arrays are suspended in air by using small custom vacuum wands made from blunt syringe needles. (**Bottom**) Magnified views show the details of the droplet shape. The narrow connectors that link each drop to the reference rail droplet equilibrate the droplet Laplace pressure, making the curvature and the height of each drop the same. Rail droplets align to hydrophilic regions in the electrode array and self-align the actuator orthogonal to the direction of motion. The reference rail droplet has a Pt wire that equilibrates the electronic potential of all the droplets with the reference rail, which, when assembled, is connected to the reference phase in the electrode array. The fluidic vias allow for the control of droplet pressure from the back.

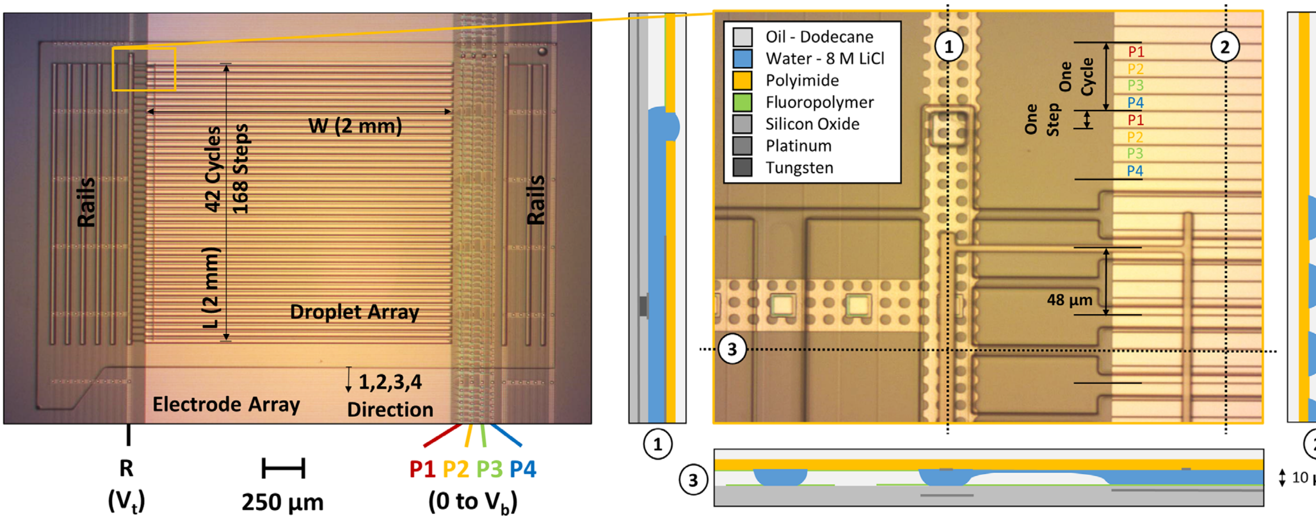

**Fig. 3. Linear actuator after assembly.** (**Left**) The entire droplet array aligned to the electrode array; electrode array phases R, P1, P2, P3, and P4 are also indicated. Phase R is biased with a negative voltage $V_t$, and phases P1 to P4 are biased with 0 V or $V_b$ as they are switched on and off. (**Right**) Magnified region of interest together with three cross-section diagrams of the actuator. All the droplets are electrically connected to the reference phase R. Cross-section 1 shows the Pt contact, which establishes this connection between the perforated phase electrode R and the reference rail droplet. Cross-section 2 is the main actuation cross section shown in Fig. 1. Cross-section 3 shows the rails and their self-alignment to the hydrophilic regions in the electrode array, shown as gaps in the green fluoropolymer. Other materials in the actuator cross sections are color-coded as indicated by the legend.

are also referred to as the top and bottom voltages, because the droplet array rides on top of the electrode array. Figure 4 shows movement frames of a high-speed actuation for both linear and rotational actuators along with top metrics achieved for this unloaded actuation (see also movies S4 and S6). During actuation, a data acquisition system measured the voltage and the current of each phase. Figure 5A shows the measured voltage and current waveforms for a linear actuation with $F_{cyc} = 250$ Hz. Current was integrated for each phase to give a charge, $Q$,

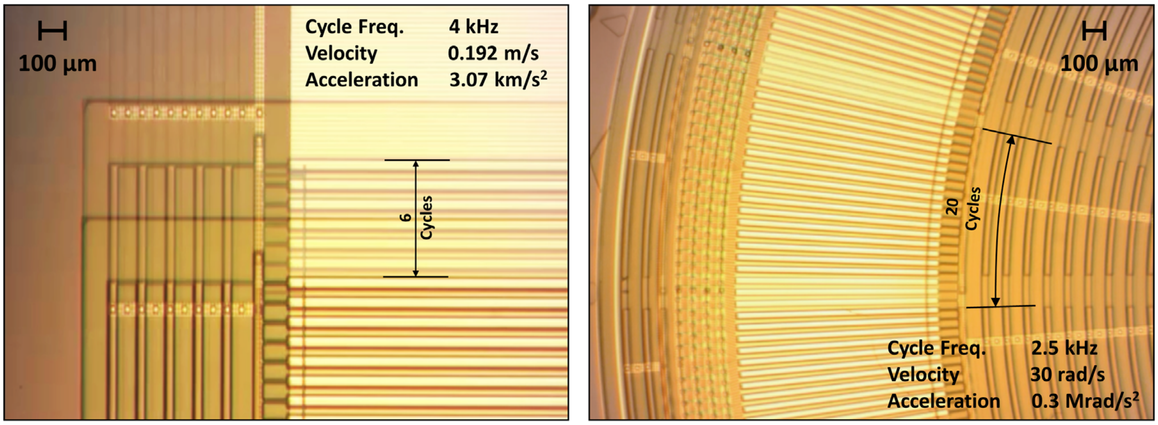

**Fig. 4. Optical micrographs of maximum velocity unloaded actuation.** (**Left**) Linear actuator moving six cycles at a cycle frequency of 4 kHz. For this actuation step, frequency is 16 kHz, velocity is 0.192 m/s, and acceleration on the first step is 3.07 km/s$^2$. (**Right**) Rotational actuator moving 20 cycles at a cycle frequency of 2.5 kHz. The maximum cycle frequency of the unloaded rotational actuator is slightly lower than the linear one because the rotational droplet width is only 1 mm, and the rails, which produce drag, form a larger relative portion of the rotational actuator. Angular velocity and acceleration corresponding to a 2.5-kHz cycle frequency are 30 rad/s (or 286 rpm) and 0.3 Mrad/s$^2$, respectively. Movies S1 to S7 show various unloaded actuations.

and the charge was normalized by the effective capacitance for each phase $C_{\text{eff}} = |C_{\text{phase}}(V_b - V_t)/V_{\text{phase}}|$, where $C_{\text{phase}}$ is the capacitance of each phase and $V_{\text{phase}}$ is the maximum applied potential for each phase. Shown in a dotted line in Fig. 5A, $Q/C_{\text{eff}}$ followed the voltage applied with a slight delay. This delay is the time difference between the electrode charging and the droplet moving onto the electrode. Figure 5B shows the product of the current and voltage waveforms or the electrical power input for each phase. Power was positive as the electrodes were charged and then negative as they were discharged. Total power for all phases was integrated, added, and divided by the number of actuation cycles to give the energy per cycle of 88 nJ. To make this energy actuator size-independent, we normalized it by the area of all the electrodes (2 mm by 2 mm) to $E_{\text{cyc}}$ of 22 mJ/m$^2$. $E_{\text{cyc}}$ is the measured electrical energy input consumed by the actuator per cycle. The maximum theoretical energy, $E_{\text{max}}$, available to a simple capacitive actuator biased at $V$ is $^1/_2CV^2$. Because of our more complex biasing scheme, which holds $V_t$ constant at a nonzero value and varies $V_b$, the maximum cycle energy is

$$E_{\max} = C\left[\left(\frac{1}{2}\right)V_b^2 - V_b V_t\right] \tag{1}$$

As expected, the measured $E_{\text{cyc}}$ never exceeded $E_{\text{max}}$ in our experiments. The contour plot of $E_{\text{max}}$ for various values of $V_t$ and $V_b$ is shown in Fig. 5C. Also plotted are the bias conditions that resulted in full actuator motion at 2.5 Hz, in open squares, and bias conditions for which the actuator was stuck at 2.5 Hz, in solid squares. For any actuation condition that resulted in full motion, for dodecane/water actuators, neither $E_{\text{max}}$ nor the measured $E_{\text{cyc}}$ substantially fell below an energy minimum of 10 mJ/m$^2$. This leads to a conclusion that 10 mJ/m$^2$ is the friction of the drops on the electrode array surface caused by contact angle hysteresis, or the hysteresis energy, $E_{\text{hyst}}$. This friction is also equivalent to an opposing force of 10 mN/m, normalized here by the total droplet width, $W_{\text{total}}$. The friction force can also be observed directly by trying to physically move the actuator with the voltages off: It was 1 ± 0.5 mN; the large uncertainty is due to the force being at the lower limit of our measurement capability, but it gives an $E_{\text{hyst}}$ range of 6 to 18 mJ/m$^2$. Figure 5D shows $E_{\text{cyc}}$ and $E_{\text{max}}$ as a function of reducing voltage $V_b$ for a 25-Hz actuation. At high $V_b$, $E_{\text{max}}$ was substantially higher than $E_{\text{cyc}}$, because the actuator was unloaded and only needed to overcome $E_{\text{hyst}}$. As $V_b$ was reduced, the available actuation energy, $E_{\text{max}}$, shrank and approached $E_{\text{hyst}}$; near the intersection of $E_{\text{max}}$ and $E_{\text{hyst}}$, the actuation stopped. At that point, the actuator did not have enough energy to overcome its internal friction. $E_{\text{cyc}}$ was roughly constant and close to the hysteresis energy until actuation stopped, at which point it quickly fell to zero. Figure 5E shows $E_{\text{cyc}}$ as a function of cycle frequency. For higher velocities, $E_{\text{cyc}}$ increased. It also increased when load was added for the same frequency. There was a consistent local minimum in $E_{\text{cyc}}$ at $F_{\text{cyc}}$ of 1 kHz; this was due to the transition from start-and-stop–type motion at each step to smoother continuous motion as velocity increased. This transition was confirmed in the $Q$ profile plots; see the Supplementary Materials for details and additional electrical data.

## Loaded actuation

Loaded characterization of a linear actuator is shown in Fig. 6. Force loading was achieved by partially pushing the droplet array off the electrode array (see Fig. 6A). As droplets moved off the electrode array, they were no longer deformed by the electrodes, and so, they did not contribute to actuation; however, they stayed attached to the fluoropolymer surface and opposed motion with the same hysteresis energy as the droplets on top of the electrode array. This was confirmed by the fact that, even when a large part of the droplet array was off the electrode array, $E_{\text{cyc}}$ never fell below $E_{\text{hyst}}$ calculated using all the drops (on and off the electrode array) for actuations that resulted in full motion. Dividing the actuator into two sections, as shown in Fig. 6A, results in a load section that has $N_{\text{load}}$ droplets and an actuator section that has $N_{\text{act}}$ droplets, with $N_{\text{load}} + N_{\text{act}} = N$, the total drop number. The load force is $E_{\text{hyst}}N_{\text{load}}W$ and is equal to the output force generated by the actuator. Output force can be further normalized by the total width of the actuating droplets, $N_{\text{act}}W$, to make it independent of actuating area, giving the output force as $E_{\text{hyst}}N_{\text{load}}/N_{\text{act}}$ in units of millinewtons per meter. As the droplet array moved off the electrode array, $N_{\text{load}}$ increased and $N_{\text{act}}$ decreased, and thus, the output/load force increased. Eventually, the load force became too great, and the actuator started skipping steps. The maximum output force was obtained at

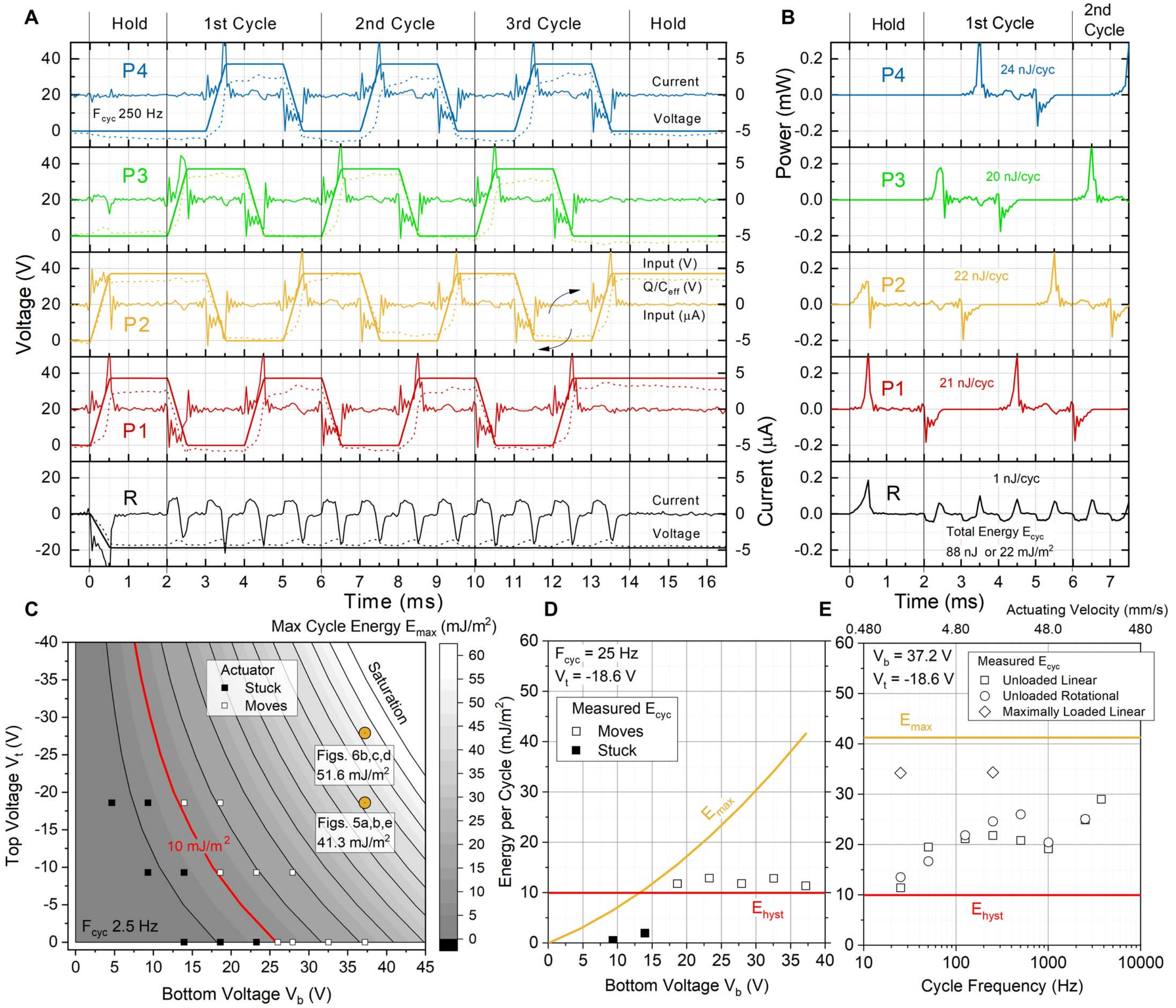

**Fig. 5. Electrical characterization of microhydraulic actuation.** (**A**) Voltage and current data for a three-cycle actuation with a cycle frequency of 250 Hz. Each graph segment shows data for a separate phase: electrode phases (P1, P2, P3, and P4) and the droplet reference phase (R). Also shown in a dotted line is the value of total electrode charge $Q$, normalized by the effective capacitance of the electrode. (**B**) Electrical power input data for each phase, calculated from the product of the voltage and the current. Integrated power averaged over the number of cycles for each electrode gives the phase energy per cycle; total cycle energy is the sum of all phase energies or 88 nJ. This can be further normalized by the active actuator area of 4 mm² to $E_{cyc}$ of 22 mJ/m². (**C**) Contour plots of the maximum cycle energy $E_{max} = C(V_b^2/2 - V_bV_t)$; the hysteresis energy, $E_{hyst}$, of 10 mJ/m² is highlighted in red. Open symbols show bias conditions that resulted in motion at a cycle frequency of 2.5 Hz; solid symbols show bias conditions that did not result in actuator motion. Also shown in orange are the bias conditions for (A), (B), and (E) and for Fig. 6 (B to D). Contact angle saturation energies are shown in white. (**D**) Measured energy per cycle $E_{cyc}$, as well as $E_{max}$ and $E_{hyst}$ as a function of $V_b$ for $F_{cyc}$ = 25 Hz actuation. (**E**) Measured cycle energy $E_{cyc}$ as a function of actuation frequency for loaded and unloaded linear actuators and unloaded rotational actuators.

different cycle frequencies, just before the actuator started to skip steps, and is plotted in Fig. 6B as a function of actuation velocity. Also shown is $E_{max}$ in units of millinewtons per meter and the expected maximum output force at low frequency, $E_{max} - E_{hyst}$. The measured maximum force matched the expected force closely but rapidly fell off as actuation velocity increased and went to zero at the maximum unloaded velocity, close to the value obtained in Fig. 4. The maximum force at low velocity was 43 mN/m. For the 2 mm–by–2 mm actuator, $W_{total}$ was 84 mm, and the output force was 3.6 mN; this was 5500 times higher than the weight of the actuator. At maximum power, the force-to-weight ratio was still an impressive 1280. Mechanical output power for any actuator is force times velocity. It can be normalized by the weight of the actuator to give the output power density. The maximum output power density calculated from actuation velocity and output force is shown in Fig. 6B. It was zero at zero velocity when the force was maximum and also zero at maximum velocity when force was

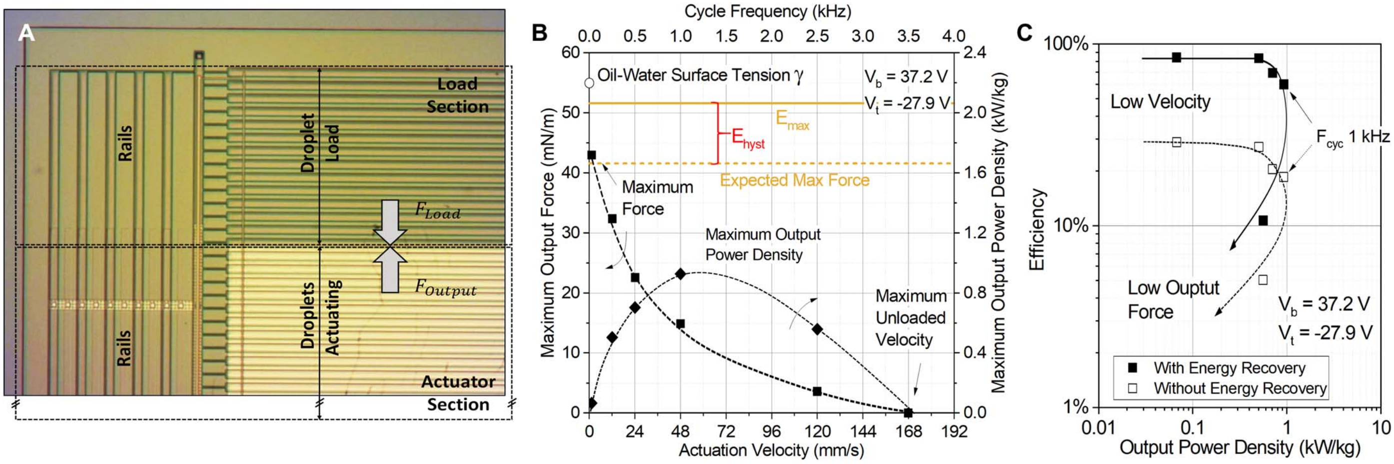

**Fig. 6. Loaded actuation.** (**A**) Optical micrograph of a linear microhydraulic actuator operating with a load. Loading is accomplished by pushing some of the droplets off the electrode array. (**B**) Left axis shows the maximum output force on the load section as a function of cycle frequency and actuation velocity. Total maximum load force is calculated from the hysteresis energy, 10 mN/m, times the total load droplet width, and then normalized by the total width of the actuating droplets, to give the loaded maximum output force in millinewtons per meter. Right axis shows the output power density at maximum load as a function of actuation velocity and cycle frequency. Output power density is calculated as the product of velocity and output force normalized by the actuator weight. (**C**) Plot of the energy conversion efficiency and output power density as cycle frequency is increased. Conversion efficiency is the mechanical energy output divided by the electrical input energy. For points with energy recovery, the electrical input energy was calculated as the integral of the current-voltage product or the electrical energy applied minus the electrical energy returned. For points without energy recovery, the electrical input energy was calculated as the integral of only the positive values of the current-voltage product or just the electrical energy applied.

zero. At $F_{cyc}$ of approximately 1 kHz, output power density reached a maximum of 0.93 kW/kg. The efficiency of actuation can be calculated from the mechanical output power divided by the measured electrical input power ($E_{cyc}F_{cyc}$). Figure 6C shows the efficiency versus power density. Efficiency was highest at low velocity and reached 83%. This is close to the estimate of $1 - E_{hyst}/E_{max}$ of 0.81. As velocity increased, efficiency dropped; at a maximum power density of 0.93 kW/kg, it became 60%. On the falling side of the power density curve, for $F_{cyc} >$ 1 kHz, both efficiency and power density rapidly decreased. Also shown in Fig. 6C is a more conservative way to calculate the efficiency: This calculation shows electrical power input calculated by ignoring all nonpositive contributions of electrical power. In essence, this ignores the power returned by the actuator as the capacitor phases are discharged. The comprehensive characterization of efficiency, mechanical output power, and electrical input power is one of the main contributions of this work. Previously (*15*), electrical power input was estimated on the basis of $CV^2$ metrics, and the mechanical power output was calculated from acceleration measurements. Thus, neither could be precisely measured as a function of actuation velocity.

### Rotational actuation

For the 10-mm-diameter rotational actuator (Fig. 4), it is impossible to push the droplet array off the electrode array in the same way, so the same force characterization techniques cannot be used. However, the force contributions per droplet width at zero velocity should be the same for linear and rotational actuators. By using the force per total droplet width of 43 mN/m measured in the linear actuator, we calculated the maximum stall torque expected in the rotational actuator as 84 mN-mm. At maximum unloaded velocity, the cycle frequencies of the actuators were not exactly the same, with 4 kHz maximum for the linear actuator and 2.5 kHz maximum for the rotational actuator. This is probably because the rotational actuator has more than double the number of alignment rails and thus has more viscous drag. Electrical data for rotational actuation are available in the Supplementary Materials.

### Comparison with muscle

Figure 7 compares output forces per cross-section area and power density profiles of a 2-mm-long linear microhydraulic actuator and a 2-mm-long muscle fiber of a dogfish based on best-fit parameters by Curtin and Woledge (*21*). The remarkable similarity between the actuation profiles further underscores the similarity in their structure and function, as discussed in (*15*). The force per cross-section area is larger for muscle, but the actuation velocity is much smaller, leading to an overall lower power density. The characteristics of dogfish muscle are similar to the characteristics of muscle of many other organisms, including humans, indicating that, even with a modestly scaled 48-μm droplet pitch, microhydraulic actuators have approximately 10 times the power density of muscle. The similarity of the actual shape of the mechanical output characteristics is still under investigation.

## DISCUSSION

### Scaling to smaller dimensions: Force, power, and efficiency

Increasing the power density of microhydraulic actuators is straightforward: Decreasing droplet pitch and height reduces the droplet mass per width quadratically, whereas force per droplet width stays constant, at approximately the surface tension. This results in a quadratic increase in force density as dimensions are reduced. The actuation velocity stays roughly constant, because the increased force is counterbalanced by increased viscous losses. This is because a linear increase in force per area of actuator layer is offset by the linear increase in sheer rate and thus viscous drag. As a result, power density, the product of force density and velocity, increases quadratically, as shown in Fig. 8.

Scaling should have little direct impact on efficiency. The main factor limiting efficiency is $E_{hyst}$, the internal friction of the actuator.

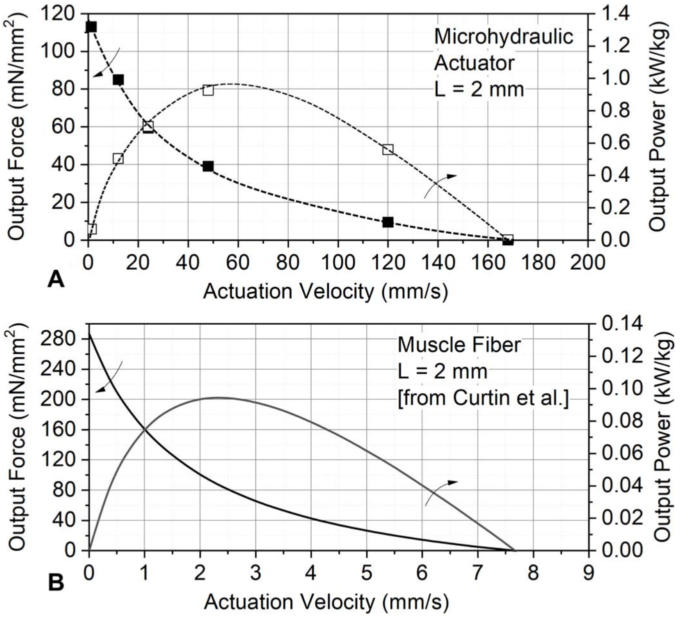

**Fig. 7. Comparison of force and power density characteristics of microhydraulic actuators and biological muscle.** (**A**) Output force and output power density characteristics of a 2-mm-long (42 droplets) microhydraulic actuator; output force was normalized by cross-section area of the actuator. (**B**) Characteristics of a 2-mm-long muscle fiber from (*21*), also normalized by fiber cross-section area. At this length, muscle fiber has a much lower actuation velocity but a higher cross-sectional force, resulting in a power density that is 10 times lower than microhydraulic actuators from Fig. 6. The shape of the characteristics is very similar.

With zero $E_{\mathrm{hyst}}$, low velocity efficiency can approach 100%. More research is required into the factors that influence $E_{\mathrm{hyst}}$; however, annealing the fluoropolymer surface before assembly reduced the $E_{\mathrm{hyst}}$ from 20 to 10 mN/m, so the surface properties of the interfaces are critical.

The power densities and efficiencies for microhydraulic actuators with 100- and 48-μm droplet pitches demonstrate the quadratic power density scaling of microhydraulic stepping actuators (Fig. 8). Projections for scaled actuators with 30- and 15-μm droplet pitches are also shown, as are various micro- and macro-actuators (*29*), including biological muscle. Metrics for 48-μm actuators presented in this work are on par with the best electric motors, and projections for 15-μm actuators beat the highest performance motors in power density at a respectable efficiency. The ultimate power density limit of microhydraulics is set by the dielectric electric field limit of the electrowetting capacitor and is well in excess of 10 kW/kg.

## Torque density, precision, and robotic applications

Many robotic applications require high-torque, medium-velocity, and high-precision motion. Microhydraulic actuators should excel in such applications. When normalized by actuator mass, the 84 mN-mm stall torque of the rotational actuator becomes a torque density of 79 Nm/kg. This is over 100 times higher than a typical torque density of a stepper motor with a similar 1-cm diameter. For example, the Emoteq HT01500 motor has a torque density of only 0.68 Nm/kg. In addition, this is not the limit of torque density for microhydraulic actuators; with scaling, torque density, like force density, increases quadratically. In the future, it is possible that robots will have microhydraulically actuated joints that have optimized torque and require no gears.

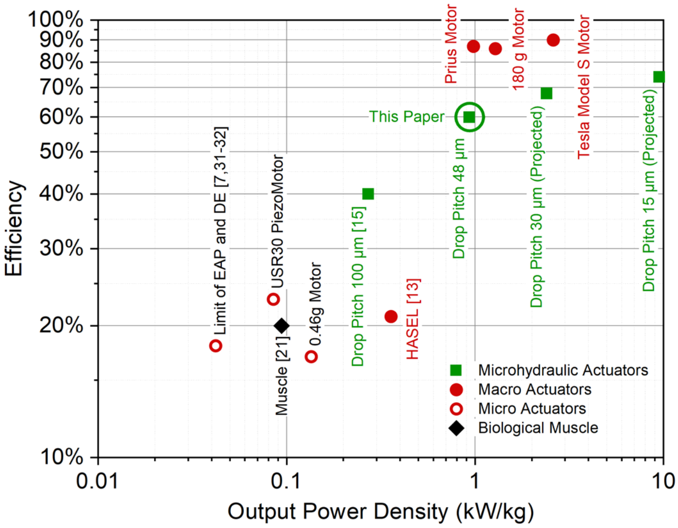

**Fig. 8. Comparison of characteristics of microhydraulic actuators to large-scale motors, micro-actuators, and biological muscle.** Microhydraulic actuators presented in this paper are 10 times more powerful than human muscle and are projected to be more powerful than the best motors with further scaling. Piezoelectric bimorph actuators and all thermal actuators are below the 10% efficiency cutoff (*29*, *30*). It is very rare for publications on electroactive polymers and dielectric elastomers to report both power density and efficiency; here, optimistically the best of each is plotted as the limit (*7*, *31*, *32*). Muscle efficiency is shown as 20%, which is the approximate conversion factor for metabolic cost to mechanical energy output in exercise machines. Data for USR30 ultrasonic motor were taken from datasheets of Shinsei Corporation, Japan. Prius and Tesla Model S motor specifications were taken from Toyota and Tesla publications for the appropriate electric vehicles.

An important characteristic of these microhydraulic actuators is the precision of their motion. Because actuation is clocked by a series of electrical pulses, the actuator moves only as many steps as it is instructed to move. Because each electrode is small, the precision and the accuracy of motion are high. For example, if the number of steps forward and backward is the same, linear actuators return to the same position to within a micrometer, even after travelling many centimeters. The linear spatial accuracy is one electrode width, or 12 μm. Similarly, rotational actuators have a precision of 0.03° and an accuracy of 0.12°. Accuracy and precision are important not only in robotics but also in many other applications, such as optomechanics. Movie S8 shows a microhydraulic rotational actuator rotating a beam-splitter cube that is over 1000 times heavier than the actuator itself.

## Technology challenges

Moving forward, several challenges stand in the way of making microhydraulic devices technologically useful. Single-layer devices are only micrometers thick, so to form a volumetric actuator with high power, multiple layers of microhydraulic material need to be integrated. Packaging is also an important challenge. Potentially, microhydraulic actuators can be completely encased in a protective coating, like metalized Mylar, similarly to how skin covers muscle. This is impossible for continuously rotating motor configurations, which could potentially be packaged with an axle that is sealed with a low–vapor pressure oil. Other technology-related challenges include reliability and temperature of operation. These challenges have already been overcome in other commercialized electrowetting technologies, such as Varioptic liquid lenses, which have an operation lifetime of years and an operational temperature range of −30° to 85°C.

## MATERIALS AND METHODS

For a more detailed description of the fabrication flow, see the Supplementary Materials and figs. S1 to S3. The electrode array was fabricated on a silicon wafer. Electrodes were implemented with two levels of interconnected platinum metal. The electrowetting dielectric on the electrodes was 1000 nm of plasma-deposited $SiO_2$ topped by 80 nm of spun-on fluoropolymer Cytop; both dielectric layers were patterned. Before assembly, photoresist was stripped with acetone and methanol, and the electrode array was annealed at 175°C for 2 min. The droplet array fabrication started with 4 μm of spun-on polyimide; one layer of platinum was patterned to help lower droplet resistivity and capped with an additional 2 μm of spun-on polyimide. Fluidic vias were etched through the polyimide, and the droplet array was coated with a fluoropolymer Cytop. The fluoropolymer layer, and some of the polyimide, was etched to define the hydrophilic droplet regions. Assembly started with wetting the droplet arrays with 8 M LiCl and peeling them off the wafer with a scalpel once free droplet arrays were placed in dodecane on top of the electrode array. Surface tension between the liquid phases was 55 $mJ/m^2$, but small amounts of contamination can lower this value. The water phase was pressurized through the fluidic via to 3.14 kPa, and the droplet and electrode arrays were brought into contact to self-align. Electrical actuation was performed using a customized PowerDNA data acquisition system from United Electronic Industries. The system is capable of high-speed analog output and simultaneous current and voltage measurement on up to seven channels in a voltage range of ±40 V, typical current measurement noise was 140 nA, and data acquisition rates up to 40 kHz were used for the highest cycle frequencies.

## SUPPLEMENTARY MATERIALS

robotics.sciencemag.org/cgi/content/full/3/22/eaat5643/DC1
Materials and Methods
Fig. S1. Top-down micrograph of the electrode array.
Fig. S2. The assembly sequence for a rotational actuator.
Fig. S3. Droplet collapse.
Fig. S4. Design of the custom output board for simultaneous current and voltage readout.
Fig. S5. Detailed electrical data for a 2 mm–by–2 mm linear actuator at different cycle frequencies.
Fig. S6. Detailed electrical data for a 2 mm–by–2 mm linear actuator at different voltages.
Fig. S7. Extended voltage, current, and power profiles at a cycle frequency of 25 Hz.
Fig. S8. Detailed electrical data for a 1-cm-diameter rotational actuator at different cycle frequencies.
Movie S1. Highly magnified linear actuation at a cycle frequency of 1.25 Hz.
Movie S2. Highly magnified linear actuation at a cycle frequency of 12.5 Hz.
Movie S3. Magnified linear actuation at a cycle frequency of 1000 Hz.
Movie S4. Magnified linear actuation at a cycle frequency of 4000 Hz.
Movie S5. Magnified rotational actuation at a cycle frequency of 125 Hz.
Movie S6. Magnified rotational actuation at a cycle frequency of 1000 Hz.
Movie S7. Rotational actuation at a cycle frequency of 1000 Hz.
Movie S8. Rotational actuation of a beam splitter cube.
Movie S9. Droplet formation video.

## REFERENCES AND NOTES

1. E. R. Laithwaite, The goodness of a machine. *Electron. Power* **11**, 101–103 (1965).
2. A. Harrington, C. M. Kroninger, "Characterization of small dc brushed and brushless motors" (ARL Tech Report ARL-TR-6389, 2013).
3. M. Karpelson, G.-Y. Wei, R. J. Wood, Driving high voltage piezoelectric actuators in microrobotic applications. *Sens. Actuators A* **176**, 78–89 (2012).
4. P. Chirarattananon, K. Y. Ma, R. J. Wood, Adaptive control of a millimeter-scale flapping-wing robot. *Bioinspir. Biomim.* **9**, 025004 (2016).
5. R. Q. Rudy, G. L. Smith, D. L. DeVoe, R. G. Polcawich, Millimeter-scale traveling wave rotary ultrasonic motors. *J. Microelectromech. Syst.* **24**, 108–114 (2015).
6. G. L. Smith, R. Q. Rudy, D. L. DeVoe, R. G. Polcawich, Integrated thin-film piezoelectric traveling wave ultrasonic motors, *16th International Solid-State Sensors, Actuators and Microsystems Conference* (*TRANSDUCERS*), Beijing, China, 5 to 9 June 2011.
7. M. Duduta, R. J. Wood, D. R. Clarke, Multilayer dielectric elastomers for fast, programmable actuation without prestretch. *Adv. Mater.* **28**, 8058–8063 (2016).
8. G. Grau, E. J. Frazier, V. Subramanian, Printed unmanned aerial vehicles using paper-based electroactive polymer actuators and organic ion gel transistors. *Microsyst. Nanoeng.* **2**, 16032 (2016).
9. F. Carpi, R. Kornbluh, P. Sommer-Larsen, G. Alici, Electroactive polymer actuators as artificial muscles: Are they ready for bioinspired applications? *Bioinspir. Biomim.* **6**, 045006 (2011).
10. A. Nespoli, S. Besseghini, S. Pittaccio, E. Villa, S. Viscuso, The high potential of shape memory alloys in developing miniature mechanical devices: A review on shape memory alloy mini-actuators. *Sens. Actuators A* **158**, 149–160 (2010).
11. M. Wehner, R. L. Truby, D. J. Fitzgerald, B. Mosadegh, G. M. Whitesides, J. A. Lewis, R. J. Wood, An integrated design and fabrication strategy for entirely soft, autonomous robots. *Nature* **536**, 451–455 (2016).
12. S. Li, D. M. Vogt, D. Rus, R. J. Wood, Fluid-driven origami-inspired artificial muscles. *Proc. Natl. Acad. Sci. U.S.A.* **114**, 13132–13137 (2017).
13. E. Acome, S. K. Mitchell, T. G. Morrissey, M. B. Emmett, C. Benjamin, M. King, M. Radakovitz, C. Keplinger, Hydraulically amplified self-healing electrostatic actuators with muscle-like performance. *Science* **359**, 61–65 (2018).
14. N. Kellaris, V. G. Venkata, G. M. Smith, S. K. Mitchell, C. Keplinger, Peano-HASEL actuators: Muscle-mimetic, electrohydraulic transducers that linearly contract on activation. *Sci. Robot.* **3**, eaar3276 (2018).
15. J. Kedzierski, E. Holihan, R. Cabrera, I. Weaver, Re-engineering artificial muscle with microhydraulics. *Microsyst. Nanoeng.* **3**, 17016 (2017).
16. J. Kedzierski, K. Meng, T. Thorsen, R. Cabrera, S. Berry, Microhydraulic electrowetting actuators. *J. Microelectromech. Syst.* **25**, 394–400 (2016).
17. A. Takei, K. Matsumoto, I. Shomoyama, Capillary motor driven by electrowetting. *Lab Chip* **10**, 1781–1786 (2010).
18. I. Moon, J. Kim, Using EWOD (electrowetting-on-dielectric) actuation in a micro conveyor system. *Sens. Actuators A* **130–131**, 537–544 (2006).
19. R. Yeh, S. Hollar, K. S. Pister, Single mask, large force and large displacement electrostatic linear inchworm motors. *J. Microelectromech. Syst.* **11**, 330–336 (2002).
20. C. Livermore, A. R. Forte, T. Lyszczarz, S. D. Umans, A. A. Ayon, J. H. Lang, A high-power MEMS electric induction motor. *J. Microelectromech. Syst.* **13**, 465–471 (2004).
21. N. A. Curtin, R. C. Woledge, Power output and force-velocity relationship of live fibres from white myotomal muscle of dogfish, *Scyliorhinus canicula*. *J. Exp. Biol.* **140**, 187–197 (1988).
22. C. J. Pennycuick, M. A. Rezende, The specific power output of aerobic muscle, related to the power density of mitochondria. *J. Exp. Biol.* **108**, 377–392 (1984).
23. G.-Z. Yang, J. Bellingham, P. E. Dupont, P. Fischer, L. Floridi, R. Full, N. Jacobstein, V. Kumar, M. McNutt, R. Merrifield, B. J. Nelson, B. Scassellati, M. Taddeo, R. Taylor, M. Veloso, Z. L. Wang, R. Wood, The grand challenges of *Science Robotics*. *Sci. Robot.* **3**, eaar7650 (2018).
24. G.-Z. Yang, P. Fischer, B. Nelson, New materials for next-generation robots. *Sci. Robot.* **2**, eaap9294 (2017).
25. Y.-P. Zhao, Y. Wang, Fundamentals and applications of electrowetting: A critical review. *Rev. Adhesion Adhesives* **1**, 114–172 (2013).
26. S. Berry, J. Kedzierski, B. Abedian, Low voltage electrowetting using thin fluoroploymer films. *J. Colloid Interface Sci.* **303**, 517–524 (2006).
27. M. R. Conde, Properties of aqueous solutions of lithium and calcium chlorides: Formulations for use in air conditioning equipment design. *Int. J. Therm. Sci.* **43**, 367–382 (2004).
28. U. Srinivasan, D. Liepmann, R. T. Howe, Microstructure to substrate self-assembly using capillary forces. *J. Microelectromech. Syst.* **10**, 17–24 (2001).
29. R. J. Wood, E. Steltz, R. S. Fearing, Nonlinear performance limits for high energy density piezoelectric bending actuators, in *Proceedings of the 2005 International Conference on Robotics and Actuation (ICRA)*, Barcelona, Spain, 18 to 22 April 2005 (IEEE, 2005), pp. 3633–3640.
30. Q.-M. Wang, X.-H. Du, B. Xu, L. E. Cross, Electromechanical coupling and output efficiency of piezoelectric bending actuators. *IEEE Trans. Ultrason. Ferroelectr. Freq. Control* **46**, 638–646 (1999).
31. K. Meijer, M. S. Rosenthal, R. J. Full, Muscle-like actuators? A comparison between three electroactive polymers. *Proc. SPIE* **4329**, 7–15 (2001).
32. J.-S. Plante, S. Dubowsky, On the properties of dielectric elastomer actuators and its implications for their design. *Smart Mater. Struct.* **16**, 227–236 (2007).

**Acknowledgments:** We thank the entire Microelectronics Laboratory staff for help with microfabrication and process development. We specifically thank M. Cook for developing the plasma etch recipes and J. Maldonado and H. Chea for lithography and polyimide processing support. We also thank I. Weaver for help with the testing setup. **Funding:** This material is based on work supported by the Assistant Secretary of Defense for Research and Engineering under Air Force contract nos. FA8721-05-C-0002 and/or FA8702-15-D-0001. Any opinions, findings, conclusions, or recommendations expressed in this material are those of the authors and do not necessarily reflect the views of the Assistant Secretary of Defense for Research and Engineering. **Author contributions:** Both authors contributed to the experimental design, methods, and validation and approved the final version of the manuscript. J.K. wrote the original draft. **Competing interests:** The authors declare that they have no competing interests. **Data and materials availability:** All data needed to evaluate the conclusions are included in the paper or the Supplementary Materials. Contact J.K. for materials, including motor datasheets cited in Fig. 8.

Submitted 12 March 2018
Accepted 1 August 2018
Published 19 September 2018
10.1126/scirobotics.aat5643

**Citation:** J. Kedzierski, E. Holihan, Linear and rotational microhydraulic actuators driven by electrowetting. *Sci. Robot.* **3**, eaat5643 (2018).

Science Robotics

# Linear and rotational microhydraulic actuators driven by electrowetting

Jakub Kedzierski and Eric Holihan

*Sci. Robot.* **3** (22), eaat5643. DOI: 10.1126/scirobotics.aat5643

---

*Science Robotics* (ISSN 2470-9476) is published by the American Association for the Advancement of Science. 1200 New York Avenue NW, Washington, DC 20005. The title *Science Robotics* is a registered trademark of AAAS.